Comparing volumetric reconstruction algorithms for light field imaging of high signal-to-noise ratio neuronal calcium transients

Carmel L. Howe,[1,2] Peter Quicke,[1,2] Pingfan Song,[3] Herman Verinaz Jadan,[3] Pier Luigi Dragotti,[3] and Amanda J. Foust[1,2]

[1] *Department of Bioengineering, Imperial College London, London, UK*
[2] *Centre for Neurotechnology, Imperial College London, London, UK*
[3] *Department of Electrical and Electronic Engineering, Imperial College London, London, UK*
[*] *a.foust@imperial.ac.uk*

Abstract: Light field microscopy (LFM) enables fast, light efficient, volumetric imaging of neuronal activity with functional fluorescence indicators. Here we apply LFM to single-cell and bulk-labeled imaging of the red calcium dye, CaSiR-1 in acute mouse brain slices. We compare two common light field volume reconstruction algorithms: synthetic refocusing and Richardson-Lucy 3D deconvolution. We compare temporal signal-to-noise ratio (SNR) and spatial signal confinement between the two LFM algorithms and conventional widefield image series. Both algorithms can resolve calcium signals from neuronal processes in three dimensions. Increasing deconvolution iteration number improves spatial signal confinement but reduces SNR compared to synthetic refocusing.

© 2020

1. Introduction

Understanding how neuronal networks learn, process, and store information requires an imaging technique capable of monitoring the activity of hundreds to thousands of neurons simultaneously. Capturing rapid neuronal network dynamics requires high temporal resolution at cellular or subcellular spatial resolution. The development of synthetic and genetically-encoded fluorescence indicators of intracellular calcium concentration [1, 2] and membrane voltage [3, 4] has the potential to enable functional imaging on these scales.

The ability to discriminate transient changes in membrane potential or calcium from baseline noise is described by the temporal signal-to-noise ratio (SNR). For most functional fluorescence applications shot noise limits the temporal SNR, and hence SNR is proportional to the square-root of the collected fluorescence photon flux. Experiments that depend on high acquisition rates and/or high SNR require the use of high photon budget imaging modalities. In particular widefield, single-photon imaging of activity indicators enables fast imaging with high photon fluxes by exciting fluorescence simultaneously in all illuminated structures. Widefield excites fluorescence efficiently throughout a volume, however, only one axial plane is imaged. In this configuration, fluorescence excited above and below the imaging plane is not only unnecessary, but contributes spurious fluorescence to the in-focus image, degrading contrast and confusing the functional signals [5].

Light field microscopy (LFM) exploits out-of-focus fluorescence simultaneously excited throughout the volume. LFM combined with widefield single-photon fluorescence excitation enables volumetric collection maximizing the photon budget. LFM is a three-dimensional (3D) imaging technique which encodes both lateral position and angular information unlike conventional imaging which focuses on objects in a single plane [6]. A microlens array (MLA)

at the microscope's native image plane enables image reconstruction at different planes and perspectives from a single light field image. This increases light efficiency and speed at the cost of spatial resolution as the cameras pixels now divide over four-dimensions (x,y,θ_x,θ_y) rather than two (x,y). The 'native LFM spatial resolution' is given by the microlens pitch divided by the objective magnification. A LFM image consists of circular subimages, Figure 1B which are parameterized by the 4D function $\mathcal{L}(u, v, x, y)$, where each lenslet is $\mathcal{L}(u, v, \cdot, \cdot)$ and the same pixel in each lenslet subimage is $\mathcal{L}(\cdot, \cdot, x, y)$. Each circular subimage represents the angular content of the light at a specific spatial location. Two main classes of algorithms for reconstructing volumes from LFM images have been described: synthetic refocusing [6] and 3D deconvolution [7]. Synthetic refocusing extracts from a light field single planes that correspond to widefield images. Multiple planes can be reconstructed orthogonal to the optical axis to generate a z-stack. Synthetic refocusing is computationally fast as each pixel in the output volume is simply the weighted sum of a subset of pixels in the light field. However, similar to widefield imaging this technique lacks optical sectioning such that out-of-focus sources reduce the contrast of in-focus sources. 3D deconvolution aims to reconstruct the volume by deconvolving its light field measurements with a 3D light field point spread function (PSF) based on a wave optics model [8]. This can be achieved by using iterative deconvolution methods, such as Richardson-Lucy [9, 10]. 3D deconvolution can achieve a higher spatial resolution than synthetic refocusing because the individual projections through the volume sample the object more finely than the microlens array, thus improving the discrimibility of signals in 3-dimensions. However, 3D deconvolution approaches are computationally intensive and amplify noise [11].

LFM's capacity to capture volumetric data from 2D frames has recently motivated its application to imaging neuronal activity in non-scattering specimens such as C. Elegans and Zebrafish [12–16]; however, there are also a few examples in mammalian brain *in vivo* [17–19]. Seeded iterative demixing [17, 19] and compressive LFM [13] increase the speed of neuronal localization and single-cell time series analysis by only identifying and localizing somatic signals. Notably, these techniques improved performance in scattering brain tissues compared to volume reconstruction methods that only account for ballistic photons. However, volume reconstruction is still required to image the generation and propagation of voltage and calcium transients through axons and dendrites over hundreds of microns.

Here, we imaged and analyzed light field time-series from neurons loaded with a red-emitting calcium dye, CaSiR-1 [20] in acute mouse brain slices. We compare temporal SNR and spatial confinement of fluorescence transients from LFM volumes synthetically refocused or 3D deconvolved from the light field time series. We also compare the temporal SNR of single planes from LFM reconstructed volumes to widefield image time series acquired from the same neurons.

2. Materials and Methods

Parts of the following methods and preliminary SNR quantification results were published in [21].

2.1. Optical System

We designed our LFM following the guidance in [6] described in more detail in [22].

Briefly, imaging was performed with a custom-built epifluorescence microscope with a MLA (125 µm pitch, f/10, RPC Photonics) placed at the imaging plane of a 25×, Numerical Aperture (NA)=1.0 water immersion objective lens (XLPLN25XSVMP, Olympus) and 180 mm tube lens (TTL180-A, Thorlabs), illustrated in Figure 1A. The MLA was imaged onto a scientific complementary metal-oxide-semiconductor (sCMOS) camera (ORCA Flash 4 V2 with Camera Link, 2048×2048 pixels, 6.5 µm pixel size, Hamamatsu) with a 1:1 relay macro lens (Nikon 60 mm f2.8 D AF Micro Nikkor Lens).

The MLA was chosen such that the lateral resolution of our LFM, given by the pitch of the MLA divided by the objective magnification, was 5 µm, roughly half the diameter of a

cortical neuron (10 µm). The axial resolution of a LFM is defined by the number of resolvable diffraction-limited spots behind each microlens [6]. Using the Sparrow criterion and assuming a peak emission wavelength of 664 nm (λ) for CaSiR-1 [20], the spot size in the camera plane is 7.64 µm. With a 125 µm pitch MLA, we are able to resolve $N_u = 13$ distinct spots under each microlens. The depth of field when synthetically refocusing is given by eq. (1), resulting in a depth of field of 6.52 µm [6] compared to 0.8 µm in a conventional widefield microscope with the same imaging parameters.

$$D = \frac{(2 + N_u)\lambda n}{2NA^2} \tag{1}$$

where n is the refractive index.

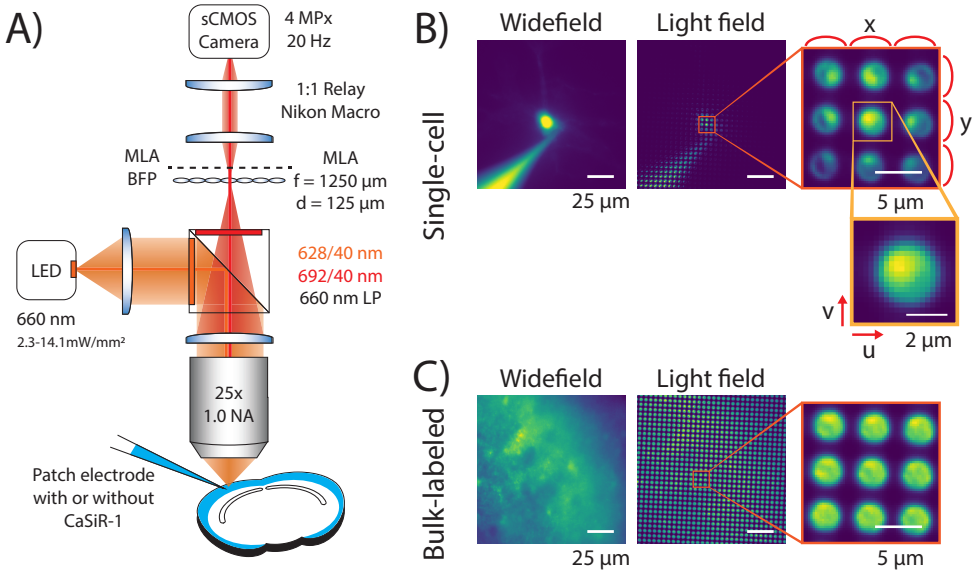

Fig. 1. A) Optical system schematic. A microlens array is placed at the native imaging plane of a widefield microscope and the back focal plane is imaged onto a sCMOS camera enabling 3D reconstructions of a 2D frame. B) Example widefield and light field images from both a single neuron intracellularly loaded with calcium dye, CaSiR-1 via a micropipette. Close up views of the raw light field images show the circular subimages encoding the 4D spatial and angular information. The light field is parameterized by a 4D function, $\mathcal{L}(u, v, x, y)$, where each lenslet is $\mathcal{L}(u, v, \cdot, \cdot)$ and the same pixel in each lenslet subimage is $\mathcal{L}(\cdot, \cdot, x, y)$. C) Example images from bulk-labeled slices where CaSiR-1 AM had been bath applied to many neurons.

2.2. Brain slice preparation

This study was carried out in accordance with the recommendations of UK Animals (Scientific Procedures) Act 1986 under Home Office Project and Personal Licenses (project license 70/9095). 400 µm slices were prepared from 33 to 196 day old mice using the 'protective recovery' method described by [23]. Slices were cut in Na-aCSF containing (in mM): 125 NaCl, 25 $NaHCO_3$, 20 glucose, 2.5 KCl, 1.25 NaH_2PO_4, 2 $MgCl_2$, 2 $CaCl_2$. After cutting, the slices were transferred for a period of 12 minutes to a solution containing (in mM) 110 N-Methyl-D glucamine, 2.5 KCl, 1.2 NaH_2PO_4, 25 $NaHCO_3$, 25 Glucose, 10 $MgCl_2$, 0.5 $CaCl_2$, adjusted to 300 – 310 mOsm/kg,

pH 7.3 – 7.4 with HCl at 36°C, before being transferred back to the first solution for at least an hour before experimental trials. All solutions were oxygenated with 95% O_2/5% CO_2.

After resting the slices were either bulk-labeled with CaSiR-1 AM-ester dye or used for single-cell labeling with CaSiR-1 potassium salt.

For bulk-labeled slices 50 µg, CaSiR-1 AM (GC402, Goryo Chemicals) [20] was dissolved in 10 µl of dimethyl sulfoxide (DMSO) with 10% w/v Pluronic F-127 (Invitrogen) and 0.5% v/v Kolliphor EL (Sigma-Aldrich) [24]. The slices were then incubated for 40 minutes at 34°C in 2 ml of Na-aCSF with the CaSiR-1 AM/DMSO mixture pipetted onto the surface of each slice, oxygenated by blowing 95% O_2/5% CO_2 onto the surface. After loading, the slices were rested in Na-aCSF for at least 20 minutes before use.

2.3. Imaging

For single-cell labeling, cortical cells were patched using 6 – 8 MOhm patch pipettes containing intracellular solution consisting of (in mM): 130 K-Gluconate, 7 KCl, 4 ATP-Mg, 0.3 GTP-Na, 10 Phosphocreatine-Na, 10 HEPES, 0.1 CaSiR-1 potassium salt (GC401, Goryo Chemicals) [20]. After sealing and breaking in, the calcium dye diffused into the cell, Figure 1B. For bulk-labeled slices (Figure 1C), cortical cells were patched containing the same intracelluar solution without the addition of the CaSiR-1 potassium salt.

Cells were patched under oblique light-emitting diode (LED) infrared illumination (peak 850 nm). The signals were recorded with a Multiclamp 700B amplifier (Axon Instruments) and digitized with a Power 1401 digitizer (Cambridge Electronic Design).

Imaging trials were taken at 20 frames/s at room temperature. Stimulation consisted of five current pulses for 10 ms at 0.5 Hz where the current was adjusted to stimulate a single action potential. For single cells, this stimulus was applied to the labeled cell with the dye-loading pipette. For bulk-labeled slices, the stimulus was applied to a cell in the field of view causing broader activation of multiple neurons in the local network. Widefield and light field trials were interleaved by removing and replacing the MLA from a precision magnetic mount. The removal and addition of the MLA shifted the focal sample plane. We calculated this focal plane shift using the thin lens equation to be ±2 µm.

Fluorescence was excited with a 660 nm LED (M660L2, Thorlabs) powered by a constant current source (Keithley Sourcemeter 1401) to illuminate the sample between 2.3-14.1 mW/mm^2. The 660 nm LED was collimated with an f = 16 mm aspheric lens (ACL25416U0-A, Thorlabs) and filtered with a 628/40 nm excitation filter (FF02-628/40, Semrock). Collected fluorescence was filtered with a 660 nm long-pass dichroic (FF660-Di02, Semrock) along with a 692/40 nm emission filter (FF01-692/40, Semrock). Imaging data were acquired with Micromanager [25].

Single-cell labeled somata laid between 46 and 49 µm below the slice surface, with a median depth of 47 [46.2, 48.6] µm. Whereas bulk-labeled somata laid between 29 and 36 µm below the slice surface, with a median depth of 34 [30, 34.8] µm.

2.4. Light field volume reconstruction

We reconstructed light field source volumes from the raw light fields (Figure1B&C) using synthetic refocusing [6] and Richardson-Lucy deconvolution [7, 9, 10]. Images synthetically refocused at a plane $f' = \alpha f_0$, where f_0 is the native focal plane, were calculated from a light field image parameterized by $\mathcal{L}(x, y, u, v)$ using the formula derived in [26] as

$$I(x, y) = \sum_{u,v} \mathcal{L}(x + u(1 - 1/\alpha), y + v(1 - 1/\alpha), u, v), \tag{2}$$

where $I(x, y)$ represents the refocused image. This process can be interpreted as a summation over different shifted angular 'views' of the sample represented by $\mathcal{L}(x, y, \cdot, \cdot)$ such that the rays forming the views intersect at the desired refocus plane. We synthetically refocused 'stacks' of

images or image time series, $I(x, y, z, t)$ by refocusing at 1 µm z-intervals using linear interpolation of the collected light field images or videos.

Stacks from the same light field images were also calculated using Richardson-Lucy deconvolution. The 3D light field PSF was calculated using the method described in [8], by considering how a light field microscope collects fluorescence from a dipole oscillating with a wavelength of 550 nm. The total PSF was calculated as an incoherent sum of dipoles oriented along x, y, and z. PSF values were calculated on a 5×5 grid relative to the microlens. A low resolution PSF was calculated by averaging over the PSF values weighted by a 2D Hamming window of a width equal to the MLA pitch and coaxial with the lens. The estimated volume, x, is recovered from the measured light field image, y, and the PSF, H using the following iterative update scheme in matrix-vector notation:

$$x^{k+1} = \frac{1}{a}\left[H^T \frac{y}{Hx^k}\right] x^k, \tag{3}$$

where the fraction y/Hx^k is computed element-wise and $a = \sum_i H(i,:)$. Stacks were reconstructed using this method as with synthetic refocusing for varying numbers of iterations of eq. 3.

2.5. Time Series Analysis

2.5.1. SNR

Signals were extracted from widefield or light field time series reconstructed with synthetic refocusing or Richardson-Lucy 3D deconvolution.

We calculated $\Delta F/F$ using eq. (4) where F was the raw fluorescent signal, F_0 was the baseline fluorescence taken as an average prior to the action potential, and F_d was the camera's dark signal (all in counts).

$$\frac{\Delta F}{F} = \frac{F - F_0}{F - F_d} \tag{4}$$

An 'activation map' was produced from the variance over time to indicate the pixels containing the greatest temporal signal from the $\Delta F/F$ map. Regions of interest (ROI) were defined by extracting the top 2 percentile of signal containing pixels (somatic and dendritic).

The SNR was calculated by dividing the peak signal (%) by the baseline noise (%), given by the square-root of the variance of the baseline fluorescence taken as an average prior to the action potential (20 samples, 1 second).

2.6. Statistics

All statistics are reported as median [inter-quartile range (IQR)]. Wilcoxon matched-pairs signed-rank test was performed between synthetically refocused and 3D deconvolved light field time series. These reconstructions were generated from the same data, removing independent variables such as bleaching and changes in dye loading in the case of single-cell labeling. Statistical analysis was performed using Python SciPy [27].

2.7. Signal Confinement

2.7.1. Spatial Profiles

To compare the spatial signal confinement spatial profiles were generated. To produce the widefield axial profile a z-stack was collected manually. At the end of an imaging trial the micropipette was removed and a z-stack was collected by moving the plane of focus through the sample between -40 to 40 µm in steps of 1 µm using a stepper motor. Light field axial profiles were generated by synthetically refocusing and deconvolving at different depths of focus from the light field taken with the cell in the native imaging plane. Lateral profiles were then generated by taking a line plot through the cell on widefield or reconstructed light field images at the plane of

best focus. The spatial signal confinement is reported from the Full-Width at Half-Maximum (FWHM). Friedman's Two-Way Analysis of Variance by Ranks was performed between the FWHMs from widefield and light field volumes reconstructed with synthetic refocusing and 3-iteration Richardson-Lucy 3D deconvolution.

The spatial profiles from single-cells were generated from either a single static image in the case of light field frames or a stack of widefield frames. However, in bulk-labeled slices the background signal was very large and the spatial profiles were generated from the activation map described in Section 3. Maximum intensity projections were taken through xy, xz, and yz.

2.7.2. Temporal Spatial Profiles

Temporal spatial profiles were produced from single cells to determine the axial spread of the calcium fluorescence response. Light field axial profiles were generated as in Section 2.7.1. Time courses were extracted for each depth from either a somatic or nearby dendritic ROI. $\Delta F/F$ was calculated using eq. 4 in Section 2.5.1. A line plot across the axial range was generated from the sum over time.

3. Results

3.1. Synthetic refocusing allows fast, high SNR light field reconstruction

We compared the performance of light field reconstruction techniques on the temporal SNR from both single-cell and bulk-labeled slices. We reconstructed volumetric light field time series from 4 single cells (Figure 2A) and 4 bulk-labeled slices (Figure 2B) with synthetic refocusing and Richardson-Lucy 3D deconvolution. For single-cell trials calcium transients were stimulated by applying small current pulses (red lines) to the soma via whole-cell patch clamp (Figure 2A2). Calcium transients from bulk-labeled slices were captured after a single cell was stimulated within the field of view (Figure 2B2). Time courses were extracted from a ROI taken from the top 2 percentile of pixels at the native focal plane, and the SNR, peak signal, and baseline noise were compared between the two light field reconstruction algorithms. Single-plane widefield time series were also extracted from matched ROIs.

Iterative 3D deconvolution algorithms including Richardson-Lucy are known to amplify noise [28] which increases with iteration number. Therefore, we quantified the effect of iteration number on the peak signal, noise, and SNR from single-cell trials. Light field time series were deconvolved with between 1 and 21 iterations. The synthetically refocused results were used as a baseline for comparison, due to the speed and relative simplicity of their reconstruction. Therefore, the deconvolved time series were normalized to synthetically refocused time series generated from the same raw light fields. On average, the peak signal (%) increases with iteration number with respect to synthetically refocused light field time series, Figure 2C1. Between 1 and 7 iterations, the deconvolved peak signal increases exponentially after which it plateaus with a peak signal around 2× greater than what is achieved from the synthetic refocusing reconstruction. In all trials, as iteration number increases the noise (%) increased compared to synthetically refocused light field time series, Figure 2C2. The deconvolved time series noise was on average the same as synthetically refocused light field time series after 1 iteration increasing to 5× greater with 21 iterations. Therefore, on average, as iteration number increases the SNR reduces, Figure 2C3. The SNR from deconvolved light field time series after 1 iteration is on average 1.5×larger than that of synthetically refocused light field time series. The SNR from deconvolved and synthetically refocused trials is the same around 9 iterations. After which, deconvolution temporal SNR decreases to half that of synthetically refocused after 21 iterations.

Next, we compared the performance of light field reconstruction techniques on the SNR from all trials for both single-cell and bulk-labeled slices. Three-iteration Richardson-Lucy deconvolution was chosen to give the best lateral signal confinement at the highest possible SNR,

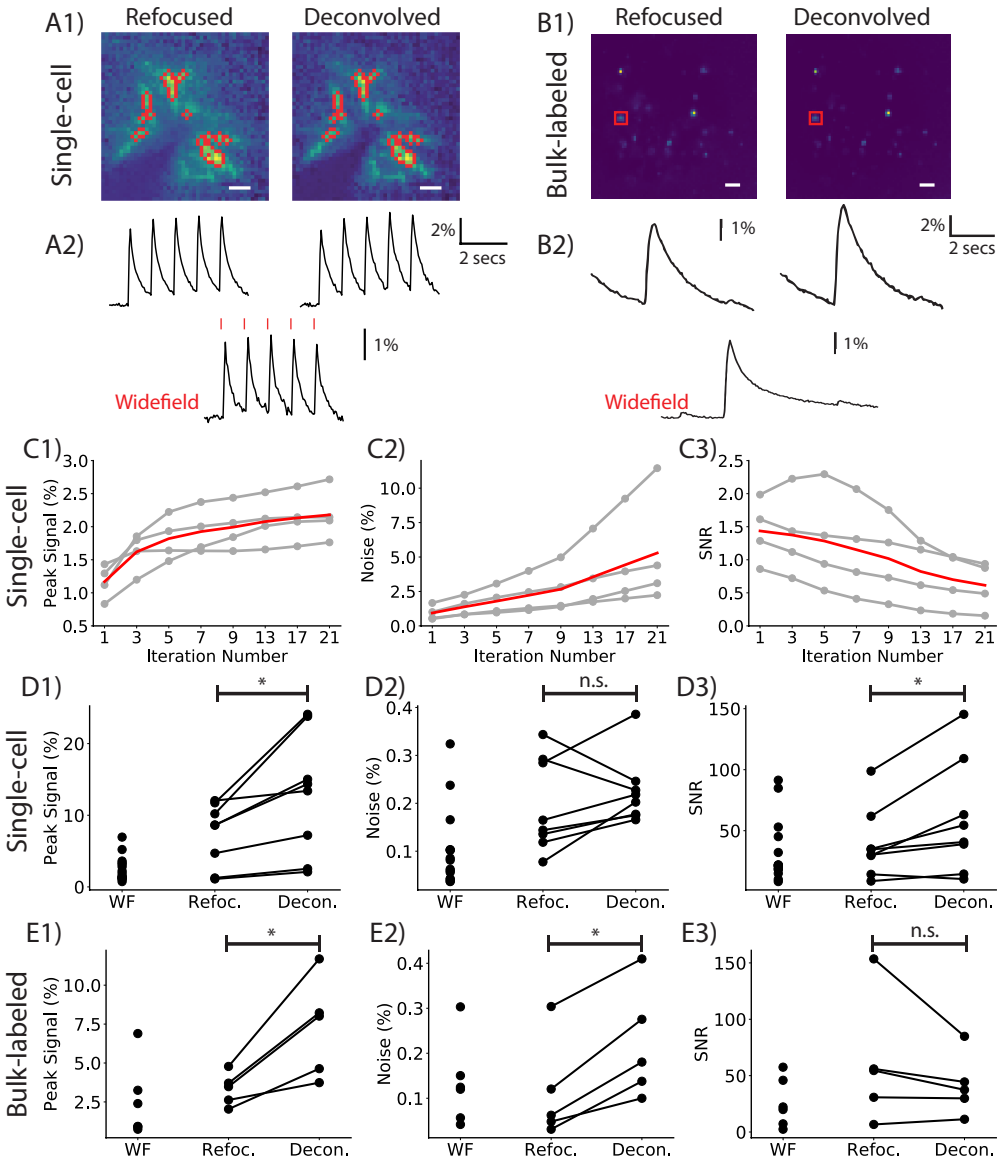

Fig. 2. How each light field reconstruction algorithm affects temporal SNR. Reconstructed planes from light fields containing single-labeled cells (A) and cells in bulk-labeled slices (B) using synthetic refocusing and 3D deconvolution (3-iteration Richardson-Lucy) algorithms. Scale bar is 25 µm for all images. Calcium transient time series (A2,B2) have been extracted from the reconstructed frame with the ROI in focus (indicated in red). As deconvolution iteration number increases, so does the peak signal (C1) and noise (C2) respective to time series reconstructed with synthetic refocusing for matching ROIs, ultimately reducing the SNR (C3). The gray traces are from separate single-cell experiments and the red line is the average. The figures are normalized to the refocused results from the same light field time series and ROIs. D1,2,3) Peak signal (%), noise (%), SNR for single-cell experiments, respectively. E1,2,3) Peak signal (%), noise (%), SNR for bulk-labeled slice experiments, respectively.

as discussed in the next section. However, higher iteration numbers further decrease SNR.

The peak signal from single-cell trials (8 trials, 4 cells, 3 mice) was significantly larger when extracted from light field time series reconstructed with three-iteration Richardson-Lucy 3D deconvolution (13.9 [2.4, 23.9]%) compared to synthetic refocusing (8.6 [1.2, 11.8]%), Figure 2D1 (Wilcoxon matched pairs signed rank, n = 8, w = 36.0, p = 0.01) and single-plane widefield time series (9 trials, 4 cells, 3 mice) (3.2 [1.7, 5.6]%).

The baseline noise was comparable between light field time series reconstructed with three-iteration 3D deconvolution (0.21 [0.17, 0.29]%) and those reconstructed with synthetic refocusing (0.15 [0.11, 0.31]%), Figure 2D2 (Wilcoxon matched pairs signed rank, n = 8, w = 28.0, p = 0.02) and those from widefield time series (0.10 [0.04, 0.26]%).

Light field time series reconstructed from single cells with three-iteration Richardson-Lucy 3D deconvolution (47.6 [13.3, 120.0]) exhibit a significantly larger SNR compared to time series reconstructed with synthetic refocusing (32.5 [12.6, 73.0]), Figure 2D3 (Wilcoxon rank sum, n = 8, w = 25.0, p = 0.03) and single-plane widefield time series (21.9 [16.8, 86.2]).

In bulk-labeled slices, the peak signal is significantly greater for light field time series reconstructed with three-iteration Richardson-Lucy 3D deconvolution (8.0 [4.1, 10.3]%) compared to synthetically refocused (3.5 [2.3, 4.4]%) (Wilcoxon rank sum, n = 5, w = 15, p = 0.04) and widefield time series (1.7 [0.8, 5.1]%), Figure 2E1 (Widefield: 5 trials, 4 cells, 2 mice. Light field: 5 trials, 4 cells, 2 mice). The baseline noise is significantly larger in three-iteration deconvolved bulk-labeled slices (0.18 [0.12, 0.35]%) compared to synthetic refocusing (0.06 [0.04, 0.23]%) (Wilcoxon rank sum, n = 5, w = 15, p = 0.04), and widefield time series (0.12 [0.05, 0.22]%), Figure 2E2. The SNR from light field time series reconstructed with synthetic refocusing (54.5 [16.3, 114.5]) is comparable to both deconvolution (37.4 [18.7, 68.7]) (Wilcoxon rank sum, n = 5, z = 2.0, p = 0.14) and corresponding widefield trials (21.1 [4.9, 51.7]), Figure 2E3.

3.2. Deconvolution reconstruction algorithms provide enhanced spatial signal confinement

Widefield excitation of fluorescent activity reporters excites fluorescence efficiently throughout a volume. However, only objects in the focal plane are in sharp focus. Therefore, fluorescence excited above and below the imaging plane contributes out-of-focus fluorescence, resulting in high background and confused functional signals. Synthetic refocusing and deconvolution volume reconstruction algorithms both have the ability to spatially localize functional signals to differing degrees. We compared the lateral and axial signal confinement of single-cells labeled with intracellular calcium dye from widefield stacks and 3D light field images (x,y,z) reconstructed with synthetic refocusing and Richardson-Lucy 3D deconvolution, Figure 3.

Two-dimensional spatial profiles were generated from widefield stacks of single-cells loaded with dye (Figure 3A1), physically refocused in 1 µm steps. Single light field images were reconstructed with synthetic refocusing (Figure 3A2) and three-iteration Richardson-Lucy 3D deconvolution (Figure 3A3). ROIs were manually selected over the soma from the 3-iteration Richardson-Lucy deconvolved light field images and used for the widefield stacks and synthetically refocused images. The lateral profiles (xy) have been plotted at the native focal plane. The red dashed lines indicate the axial profile locations (xz, yz). The axial profiles cover a depth of -40 to +40 µm.

First, we wanted to understand the effect of deconvolution iteration number on the spatial signal confinement. A line plot was taken through the lateral and axial profiles and the FWHM was calculated for both of the reconstruction algorithms from three cells. Both the lateral (Figure 3B1) and axial (Figure 3B2) signal confinement increase with increasing deconvolution iteration number. The FWHM for each deconvolution iteration has been normalized to that from synthetic refocusing, and the red line is the average for the three cells. The lateral signal confinement (Figure 3B1) for one deconvolution iteration is 1.6× better than synthetically refocused light field

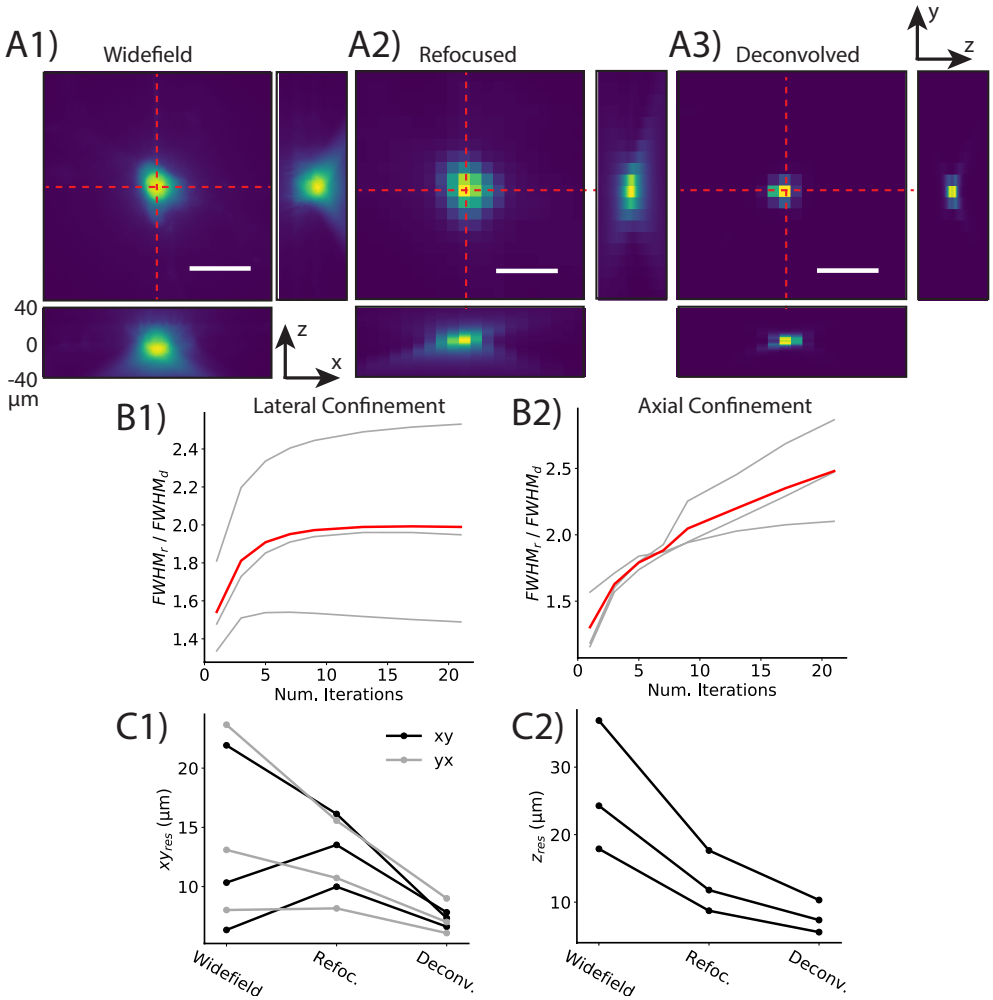

Fig. 3. Deconvolution enhances spatial signal confinement compared to widefield stacks and light field volumes reconstructed with synthetic refocusing. Lateral and axial profiles from a single-cell filled with CaSiR-1 dye have been generated. The lateral profiles have been plotted at the native focal plane from widefield stacks (A1), and light field volumes reconstructed with synthetic refocusing (A2) and 3-iteration Richardson-Lucy deconvolution (A3). The axial profiles have been extracted from the lateral positions indicated (red dashed line) and range from -40 to +40 µm. Scale bars are 25 µm. Increasing deconvolution iteration number increases both the lateral (B1) and axial (B2) signal confinement compared to synthetically refocused volumes. The deconvolved FWHM has been normalized to that of synthetic refocusing. The gray lines are from three different cells and the red line is the average. Signals are more laterally (C1) and axially (C2) confined from deconvolved light field volumes compared to both widefield and synthetically refocused light field volumes.

images and plateaus around 7 iterations with a 2× improvement. The axial signal confinement (Figure 3B2) for one deconvolution iteration is 1.4× better than synthetic refocusing increasing to 2.5× after 21 deconvolution iterations. Three-iteration Richardson-Lucy deconvolution was chosen for further analysis as it maximized lateral confinement with a high SNR.

The 2D spatial profiles (Figure 3A1-3)) clearly show that the light field images reconstructed with 3D deconvolution have finer spatial signal confinement, both laterally and axially compared

to both those reconstructed with synthetic refocusing and widefield stacks. The spatial profile for refocused volumes looks similar to widefield, which is expected due to the nature of the reconstruction. A line plot was taken through the lateral and axial profiles, and the FWHM was calculated for each of the imaging configurations from 3 cells, Figure 3C1&2). The results are summarized in Table 1.

The lateral signal confinement (xy & yx, Figure 3C1) from light field images reconstructed with 3D deconvolution (3-iteration Richardson-Lucy) is comparable to both light field images reconstructed with synthetic refocusing and widefield stacks (Friedman's Two-Way Analysis of Variance by Ranks; xy: n=3, w=2.67, p = 0.26 yx: n=3, w=4.67, p = 0.10). Additionally, light field images reconstructed with 3D deconvolution (3-iteration Richardson-Lucy) exhibit a significantly greater axial signal confinement (xz, Figure 3C2) than both light field images reconstructed with synthetic refocusing and widefield stacks (Friedman's Two-Way Analysis of Variance by Ranks; n=3, w=6, $p < 0.05$).

Table 1. Summary of FWHM from single-cell labeled spatial profiles. Reported as median [IQR], n=3. *3-iteration Richardson-Lucy.

	Widefield	Refocused	Deconvolved*	
xy	10.3 [7.1, 19.6]	13.5 [10.7, 15.6]	7.3 [6.8, 7.7]	µm
yx	13.1 [9.0, 21.6]	10.7 [8.7, 14.6]	7.0 [6.3, 8.6]	µm
xz	17.9 [19.2, 34.4]	11.8 [9.3, 16.5]	7.4 [5.9, 9.7]	µm

For the bulk-labeled slices, the out-of-focus raw fluorescence prevented resolution of individual cells. Instead the spatial profiles were generated from an activation map which was the variance over time, Figure 4. Maximum intensity projections through xz and yz were generated. The signal confinement for both synthetically refocused and 3D deconvolved light field volumes enabled resolution of a number of active neurons across different focal planes spanning 60 µm, which is unachievable with any widefield imaging system. The center of mass of each neuron ranges from -5 to +4 µm. The image contrast is higher for 3D deconvolved planes.

3.3. Light field microscopy resolves calcium signals from neuronal processes in 3D

Light field microscopy enables single-frame 3D imaging; therefore, we investigated its application to resolving calcium signals from neuronal processes in three spatial dimensions. We reconstructed 4D (x,y,z,t) light field volumes from time series and extracted temporal signals from ROIs manually defined over the cell soma and two neuronal processes from the $\Delta F/F$ map.

Depth-time plots were extracted from ROIs taken from light field time series reconstructed with synthetic refocusing (Figure 5B) and 3D deconvolution (3-iteration Richardson-Lucy, Figure 5C); unachievable with widefield microscopy (Figure 5A).

Somatic calcium transients can be seen across multiple planes in light field time series reconstructed with synthetic refocusing (Figure 5B2) and 3D deconvolution (Figure 5C2). The signal as a function of depth has been summed over time, Figure 5D1. The somatic peak signal is greater in deconvolved volumetric light field time series compared to those synthetically refocused, in agreement with the results from Section 3.

The increase in peak signal seen at the extremes of the axial range in deconvolved light field volumes is an artifact of the deconvolution algorithm and how the signal is calculated (eq. 4). The low baseline fluorescence and small dark signal is overpowered by the large out-of-focus dendritic fluorescent signal.

The peak signal seen in both the processes is greater in deconvolved volumetric light field

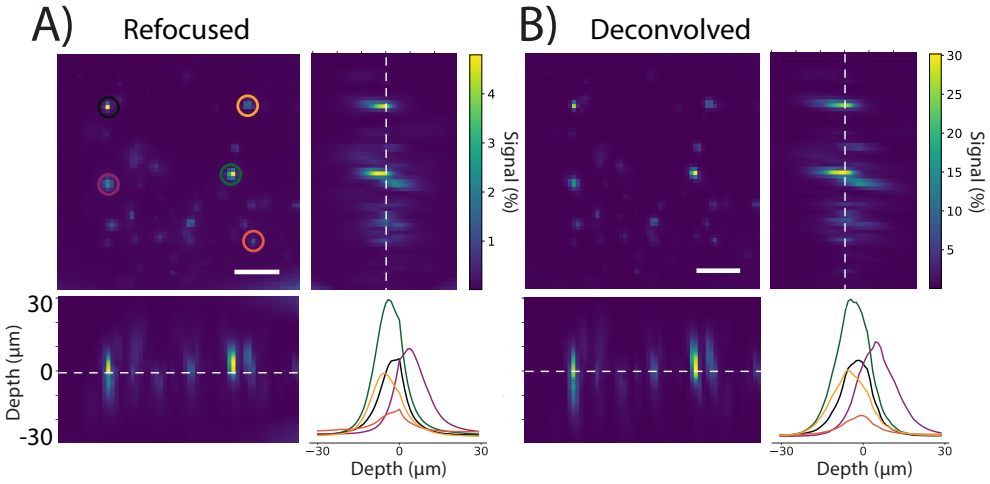

Fig. 4. Reconstructed light field volumes can distinguish cells from different axial planes in bulk-labeled slices. Planes from bulk-labeled slices were reconstructed from light field volumes with synthetic refocusing (A) and 3D deconvolution (B, 3-iteration Richardson-Lucy) between -30 and +30 µm in steps of 1 µm. Raw reconstructed light field volumes have low contrast. An activation map was generated from the variance over time to resolve active neurons. A maximum intensity projection through z was generated. A xz and yz maximum intensity projection shows multiple cells in the field of view spanning different axial planes made clearer with line profiles taken from somatic ROIs. The center of mass of each neuron ranges from -5 to +4 µm. Scale bars are 50 µm.

time series, Figure 5C3,4 compared to those synthetically refocused, Figure 5B3,4, in agreement with the results from Section 3. From the depth plots it appears that the center of mass from both of the dendrite ROIs lie close to the native focal plane (~5 µm) whereas the soma signal peaks at about 10 microns superficial to the native focal plane (Figure 5D2,3). This indicates that calcium transients can be resolved from neuronal processes in axially distinct planes.

The decay time, measured by the FWHM of somatic calcium transients at the native focal plane is the same between widefield (0.23 [0.20, 0.27]s, n=3 cells) and light field time series reconstructed with synthetic refocusing (soma: 0.24 [0.21, 0.32]s, n=3 cells) and 3D deconvolution (soma: 0.22 [0.20, 0.40]s, n=3 cells). Moreover, there is no significant difference between the decay time of somatic and dendritic signals of synthetically refocused (dendrite: 0.139 [0.136, 0.141]s, n=3 cells) or deconvolved (dendrite: 0.132 [0.126, 0.167]s, n=3 cells) light field time series.

4. Discussion

We resolved CaSiR-1 fluorescence transients in single-cells and bulk-labeled live mouse brain slices. We found that calcium transient temporal SNR from bulk-labeled slices did not differ between widefield and light field time series reconstructed with synthetic refocusing and three-iteration Richardson-Lucy 3D deconvolution. However, for single-labeled cells the SNR was significantly larger for light field time series reconstructed with three-iteration Richardson-Lucy 3D deconvolution compared to synthetic refocusing. Increasing the number of deconvolution iterations increased signal size and noise but reduced SNR. However, increased iteration number also increased axial confinement. Both light field reconstruction algorithms, synthetic refocusing and Richardson-Lucy deconvolution, enabled 3D localization of calcium transients in single dye-loaded neurons and bulk-labeled slices.

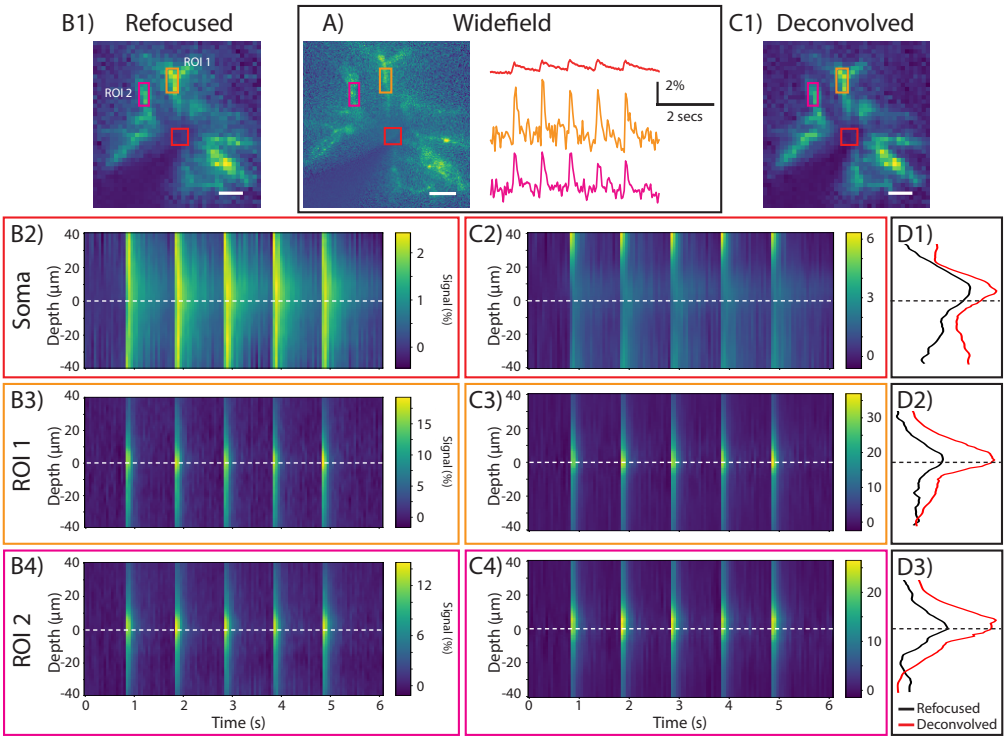

Fig. 5. Calcium signals in neuronal processes can be observed across axially distinct planes from single-cell light field volumes. A) Widefield image with time courses extracted from a somatic ROI at the focal plane and two from nearby processes. Depth-time plots have been generated from a single light field time series reconstructed with synthetic refocusing (B) and 3D deconvolution (C) taken from a somatic ROI (B2 ,C2) and two from nearby cellular processes (B3,4, C3,4). Scale bars are 25 µm. Sum of the signal over time as a function of depth from the soma (D1) and the cellular processes (D2,3). The second ROI (D3) indicates that the process may be slightly superficial to the native focal plane.

The reduction in SNR seen from deconvolved volumes arises from noise amplification due to lack of regularization [28]. To reduce noise amplification, fewer iteration numbers provide a regularizing effect on the deconvolution [11]. Richardson-Lucy deconvolution at high iteration numbers decreases temporal SNR, and moreover vastly increases computational cost compared to synthetic refocusing. However, the improved lateral and axial signal confinement may still motivate its use. We have shown that 3D deconvolution achieves higher spatial signal confinement than synthetic refocusing. Therefore, to resolve fine objects and ensure accurate spatial signal confinement a computationally expensive and time-consuming iterative deconvolution techniques could be beneficial.

Deconvolution algorithms are able to leverage the fine sampling of individual projections through the volume, whereas refocusing cannot. Here we used a coarse deconvolution approach. Lateral oversampling can further improve the lateral signal confinement, providing lateral sampling rates greater than the native LFM resolution. However, oversampling increases computational cost and was unnecessary here as the LFM was designed for cellular resolution. We used the original light field microscope design [6]. Fourier light field microscopy, where the microlens array is placed at the aperture stop of the microscope objective instead of the image

plane, has also been shown to improve the lateral sampling rate even in the degenerate native focal plane [29–31].

Both these light field reconstruction algorithms rely on ballistic photons, limiting their application in highly scattering mammalian brains. To minimize scattering, we used a red-emitting calcium dye, CaSiR-1 whose emission is less scattered than shorter wavelength emitting fluorophores. Furthermore, deep near-infrared indicators can be combined with blue-light sensitive opsins to achieve spectrally cross-talk free all-optical neurophysiology [32, 33] or combined with shorter wavelength emitting fluorophores for imaging in multiple spectral channels [34]. Despite this, all the cells in this study were relatively superficial, within the photon mean free path. Methods to improve performance in scattering tissue have been demonstrated by computationally extracting fluorescence sources [13, 17, 19, 35], or by combining the principles of confocal microscopy with LFM [36].

To deconvolve the light field volumes, our computer (Processor i7 CPU @ 3.6 GHz, RAM 32 GB) took around 1 second per iteration per frame. A typical time series consisted of 200 frames (20 Hz for 10 seconds). Therefore, the high-performance computing cluster at Imperial College London was required. Methods to increase speed without the need to use high performance computing are desirable. Reconstruction speed has been improved by a number of groups [14, 18, 37, 38].

We detected dendritic calcium activity in intracellularly dye loaded single-cells. The quality of the dye loading, however, precluded activity detection in distant processes. Calcium indicators have a much higher SNR; therefore, incorporating a genetically encoded calcium indicator (GECI) may allow tracing of functional signals through dendrites in three-dimensions or synaptic mapping. Similar analyses have been performed for sparsely labeled genetically encoded voltage indicators (GEVIs) with much lowwe baseline fluorescence, $\Delta F/F$, and temporal SNR compared to that of the CaSIR-1 calcium dye examined here. This study nonetheless also demonstrated axial resolution of functional signals from dendrites at different depths [22, 39]. Together these studies can indicate the capabilities of LFM for functional fluorescence imaging with low and high brightness indicators.

LFM's ability to instantaneously capture 3D information results in reduced imaging time and bleaching compared to widefield. Generating similar 3D volumes in widefield would require physical refocusing of the objective in between trials.

These results demonstrate the capabilities and limitations of two main light field reconstruction algorithms for high SNR functional fluorescence imaging. This shows that light field microscopy is well suited to high frame rate, superficial imaging of fluorescent indicators in the mammalian brain due to the high photon budget and ability to spatially resolve neurons and functional signals in three-dimensions.

Acknowledgements

The authors would like to thank Yu Liu, Simon Schultz, and Ann Go for their technical assistance. The authors would also like to thank the Imperial College Research Computing Service.

This project was funded by the Biotechnology and Biological Sciences Research Council (BB/R009007/1). National Institutes of Health (U01NS090501, U01NS099573, U01MH109091); Wellcome Trust Seed Award (201964/Z/16/Z); and a Royal Academy of Engineering Research Fellowship (RF1415/14/26).

Author Contributions

CLH, PQ, and AJF conceived and designed the experiments. CLH and AJF designed the light field optics. CLH performed experiments. CLH, PQ, and AJF designed the analysis. PQ, PS, HVJ, and PLD developed the deconvolution approach. CLH analyzed the data and wrote the paper. All authors contributed to manuscript revision and approved the final manuscript.

Disclosures

The authors declare no conflicts of interest.

References

1. H. Dana, B. Mohar, Y. Sun, S. Narayan, A. Gordus, J. P. Hasseman, G. Tsegaye, G. T. Holt, A. Hu, D. Walpita *et al.*, "Sensitive red protein calcium indicators for imaging neural activity," Elife **5**, e12727 (2016).
2. M. Z. Lin and M. J. Schnitzer, "Genetically encoded indicators of neuronal activity," Nat. neuroscience **19**, 1142 (2016).
3. J. Platisa and V. A. Pieribone, "Genetically encoded fluorescent voltage indicators: are we there yet?" Curr. opinion neurobiology **50**, 146–153 (2018).
4. V. Grenier, B. R. Daws, P. Liu, and E. W. Miller, "Spying on neuronal membrane potential with genetically targetable voltage indicators," J. Am. Chem. Soc. **141**, 1349–1358 (2019).
5. M. A. Popovic, N. Carnevale, B. Rozsa, and D. Zecevic, "Electrical behaviour of dendritic spines as revealed by voltage imaging," Nat. Commun. **6** (2015).
6. M. Levoy, R. Ng, A. Adams, M. Footer, and M. Horowitz, "Light field microscopy," ACM SIGGRAPH 2006 Pap. on - SIGGRAPH '06 p. 924 (2006).
7. M. Broxton, L. Grosenick, S. Yang, N. Cohen, A. Andalman, K. Deisseroth, and M. Levoy, "Wave optics theory and 3-D deconvolution for the light field microscope," Opt. Express **21**, 25418 (2013).
8. P. Quicke, C. L. Howe, P. Song, H. V. Jadan, P. L. Dragotti, T. Knopfel, A. J. Foust, S. R. Schultz, and M. Neil, "Calculation of high numerical aperture lightfield microscope point spread functions," in *Computational Optical Sensing and Imaging,* (Optical Society of America, 2019), pp. CW4A–2.
9. W. H. Richardson, "Bayesian-Based Iterative Method of Image Restoration*," J. Opt. Soc. Am. **62**, 55 (1972).
10. L. B. Lucy, "An iterative technique for the rectification of observed distributions," The Astron. J. **79**, 745 (1974).
11. M. Bertero, P. Boccacci, and V. Ruggiero, *Inverse Imaging with Poisson Data* (IOP Publishing, Bristol, 2018).
12. R. Prevedel, Y. G. Yoon, M. Hoffmann, N. Pak, G. Wetzstein, S. Kato, T. Schrödel, R. Raskar, M. Zimmer, E. S. Boyden, and A. Vaziri, "Simultaneous whole-animal 3D imaging of neuronal activity using light-field microscopy," Nat. Methods **11**, 727–730 (2014).
13. N. C. Pégard, H.-Y. Liu, N. Antipa, M. Gerlock, H. Adesnik, and L. Waller, "Compressive light-field microscopy for 3D neural activity recording," Optica **3**, 517 (2016).
14. L. Cong, Z. Wang, Y. Chai, W. Hang, C. Shang, W. Yang, L. Bai, J. Du, K. Wang, and Q. Wen, "Rapid whole brain imaging of neural activity in freely behaving larval zebrafish (Danio rerio)," eLife **6** (2017).
15. M. A. Taylor, T. Nöbauer, A. Pernia-Andrade, F. Schlumm, and A. Vaziri, "Brain-wide 3d light-field imaging of neuronal activity with speckle-enhanced resolution," Optica **5**, 345–353 (2018).
16. S. Aimon, T. Katsuki, T. Jia, L. Grosenick, M. Broxton, K. Deisseroth, T. J. Sejnowski, and R. J. Greenspan, "Fast near-whole–brain imaging in adult drosophila during responses to stimuli and behavior," PLoS biology **17**, e2006732 (2019).
17. T. Nöbauer, O. Skocek, A. J. Pernía-Andrade, L. Weilguny, F. Martínez Traub, M. I. Molodtsov, and A. Vaziri, "Video rate volumetric Ca2+ imaging across cortex using seeded iterative demixing (SID) microscopy," Nat. Methods **14**, 811–818 (2017).
18. L. M. Grosenick, M. Broxton, C. K. Kim, C. Liston, B. Poole, S. Yang, A. S. Andalman, E. Scharff, N. Cohen, O. Yizhar *et al.*, "Identification of cellular-activity dynamics across large tissue volumes in the mammalian brain," bioRxiv p. 132688 (2017).
19. O. Skocek, T. Nöbauer, L. Weilguny, F. Martínez Traub, C. N. Xia, M. I. Molodtsov, A. Grama, M. Yamagata, D. Aharoni, D. D. Cox, P. Golshani, and A. Vaziri, "High-speed volumetric imaging of neuronal activity in freely moving rodents," Nat. Methods **15**, 1–4 (2018).
20. T. Egawa, K. Hanaoka, Y. Koide, S. Ujita, N. Takahashi, Y. Ikegaya, N. Matsuki, T. Terai, T. Ueno, T. Komatsu *et al.*, "Development of a far-red to near-infrared fluorescence probe for calcium ion and its application to multicolor neuronal imaging," J. Am. Chem. Soc. **133**, 14157–14159 (2011).
21. C. L. Howe, P. Quicke, P. Song, H. V. Jadan, P. L. Dragotti, and A. J. Foust, "Comparing wide field to 3d light field for imaging red calcium transients in mammalian brain," in *Optics and the Brain,* (Optical Society of America, 2020), pp. BTu2C–4.
22. P. Quicke, C. L. Howe, P. Song, H. V. Jadan, C. Song, T. Knöpfel, M. Neil, P. L. Dragotti, S. R. Schultz, and A. J. Foust, "Subcellular resolution three-dimensional light-field imaging with genetically encoded voltage indicators," Neurophotonics **7**, 1 – 19 (2020).
23. J. T. Ting, B. Kalmbach, P. Chong, R. de Frates, C. D. Keene, R. P. Gwinn, C. Cobbs, A. L. Ko, J. G. Ojemann, R. G. Ellenbogen *et al.*, "A robust ex vivo experimental platform for molecular-genetic dissection of adult human neocortical cell types and circuits," Sci. reports **8**, 1–13 (2018).
24. R. Franconville, G. Revet, G. Astorga, B. Schwaller, and I. Llano, "Somatic calcium level reports integrated spiking activity of cerebellar interneurons in vitro and in vivo," J. neurophysiology **106**, 1793–1805 (2011).
25. A. D. Edelstein, M. A. Tsuchida, N. Amodaj, H. Pinkard, R. D. Vale, and N. Stuurman, "Advanced methods of microscope control using μManager software." J. biological methods **1**, 10 (2014).

26. R. Ng, M. Levoy, M. Brédif, G. Duval, M. Horowitz, and P. Hanrahan, "Light Field Photography with a Hand-Held Plenoptic Camera – Stanford Tech Report CTSR 2005-02," Tech. rep. (2005).
27. P. Virtanen, R. Gommers, T. E. Oliphant, M. Haberland, T. Reddy, D. Cournapeau, E. Burovski, P. Peterson, W. Weckesser, J. Bright, S. J. van der Walt, M. Brett, J. Wilson, K. Jarrod Millman, N. Mayorov, A. R. J. Nelson, E. Jones, R. Kern, E. Larson, C. Carey, İ. Polat, Y. Feng, E. W. Moore, J. Vand erPlas, D. Laxalde, J. Perktold, R. Cimrman, I. Henriksen, E. A. Quintero, C. R. Harris, A. M. Archibald, A. H. Ribeiro, F. Pedregosa, P. van Mulbregt, and S. . . Contributors, "SciPy 1.0: Fundamental Algorithms for Scientific Computing in Python," Nat. Methods **17**, 261–272 (2020).
28. N. Dey, L. Blanc-feraud, C. Zimmer, P. Roux, Z. V. I. Kam, A. Group, I. Is, L. Bp, and S. Antipolis, "Richardson-Lucy Algorithm with Total Variation Regularization for 3D Confocal Microscope Deconvolution," Microsc. Res. & Tech. **69**, 260–266 (2006).
29. C. Guo, W. Liu, X. Hua, H. Li, and S. Jia, "Fourier light-field microscopy," Opt. Express **27**, 25573–25594 (2019).
30. A. Stefanoiu, G. Scrofani, G. Saavedra, M. Martínez-Corral, and T. Lasser, "What about computational super-resolution in fluorescence fourier light field microscopy?" Opt. Express **28**, 16554–16568 (2020).
31. F. L. Liu, G. Kuo, N. Antipa, K. Yanny, and L. Waller, "Fourier diffuserscope: single-shot 3d fourier light field microscopy with a diffuser," arXiv preprint arXiv:2006.16343 (2020).
32. J. Akerboom, N. Carreras Calderón, L. Tian, S. Wabnig, M. Prigge, J. Tolö, A. Gordus, M. B. Orger, K. E. Severi, J. J. Macklin *et al.*, "Genetically encoded calcium indicators for multi-color neural activity imaging and combination with optogenetics," Front. molecular neuroscience **6**, 2 (2013).
33. N. S. Soor, P. Quicke, C. L. Howe, K. T. Pang, M. A. Neil, S. R. Schultz, and A. J. Foust, "All-optical crosstalk-free manipulation and readout of chronos-expressing neurons," J. physics D: Appl. physics **52**, 104002 (2019).
34. M. Oheim, M. van't Hoff, A. Feltz, A. Zamaleeva, J.-M. Mallet, and M. Collot, "New red-fluorescent calcium indicators for optogenetics, photoactivation and multi-color imaging," Biochimica et Biophys. Acta (BBA)-Molecular Cell Res. **1843**, 2284–2306 (2014).
35. P. Song, H. V. Jadan, C. L. Howe, P. Quicke, A. J. Foust, and P. L. Dragotti, "3d localization for light-field microscopy via convolutional sparse coding on epipolar images," IEEE Transactions on Comput. Imaging **6**, 1017–1032 (2020).
36. Z. Zhang, L. Bai, L. Cong, P. Yu, T. Zhang, W. Shi, F. Li, J. Du, and K. Wang, "Imaging volumetric dynamics at high speed in mouse and zebrafish brain with confocal light field microscopy," Nat. Biotechnol. pp. 1–10 (2020).
37. H. Li, C. Guo, D. Kim-Holzapfel, W. Li, Y. Altshuller, B. Schroeder, W. Liu, Y. Meng, J. B. French, K.-I. Takamaru, M. A. Frohman, and S. Jia, "Fast, volumetric live-cell imaging using high-resolution light-field microscopy," Biomed. Opt. Express **10**, 29 (2019).
38. N. Cohen, S. Yang, A. Andalman, M. Broxton, L. Grosenick, K. Deisseroth, M. Horowitz, and M. Levoy, "Enhancing the performance of the light field microscope using wavefront coding," Opt. express **22**, 24817–24839 (2014).
39. P. Quicke, C. Song, E. J. McKimm, M. M. Milosevic, C. L. Howe, M. Neil, S. R. Schultz, S. D. Antic, A. J. Foust, and T. Knöpfel, "Single-neuron level one-photon voltage imaging with sparsely targeted genetically encoded voltage indicators," Front. cellular neuroscience **13**, 39 (2019).